

STORM: Segment, Track, and Object Re-Localization from a Single Image

Yu Deng^{1*}, Teng Cao^{1*}, Hikaru Shindo¹, Jiahong Xue¹, Quentin Delfosse¹, Kristian Kersting^{1,2,3,4}

¹Department of Computer Science, Technical University of Darmstadt, Germany

²Hessian Center for Artificial Intelligence (hessian.AI), Germany

³German Research Center for Artificial Intelligence (DFKI), Germany

⁴Centre for Cognitive Science, Technical University of Darmstadt, Germany

yu.deng@stud.tu-darmstadt.de, teng.cao@stud.tu-darmstadt.de, hikaru.shindo@tu-darmstadt.de, jiahong.xue@stud.tu-darmstadt.de, quentin.delfosse@tu-darmstadt.de, kersting@tu-darmstadt.de

Abstract

Accurate 6D pose estimation and tracking are fundamental capabilities for physical AI systems such as robots. However, existing approaches typically require a pre-defined 3D model of the target and rely on a manually annotated segmentation mask in the first frame, which is labor-intensive and leads to reduced performance when faced with occlusions or rapid movement. To address these limitations, we propose STORM (Segment, Track, and Object Re-localization from a single iMAGE), an open-source robust real-time 6D pose estimation system that requires no manual annotation. STORM employs a novel three-stage pipeline combining vision-language understanding with feature matching: contextual object descriptions guide localization, self-cross-attention mechanisms identify candidate regions, and produce precise masks and 3D models for accurate pose estimation. Another key innovation is our automatic re-registration mechanism that detects tracking failures through feature similarity monitoring and recovers from severe occlusions or rapid motion. STORM achieves state-of-the-art accuracy on challenging industrial datasets featuring multi-object occlusions, high-speed motion, and varying illumination, while operating at real-time speeds without additional training. This annotation-free approach significantly reduces deployment overhead, providing a practical solution for modern applications, such as flexible manufacturing and intelligent quality control. **Code:** <https://github.com/dengyufuqin/Storm>

1 Introduction

Estimating the rigid six-degree-of-freedom (6D) transformation between an object and the camera—also known as object pose estimation—is a critical task in robotic manipulation (Kappler et al. 2018; Wen et al. 2022) and augmented reality (Marchand, Uchiyama, and Spindler 2015). Despite recent significant advances (He et al. 2020, 2021; Labbé et al. 2020; Park, Patten, and Vincze 2019; Wen et al. 2020), current methods face critical limitations that restrict their deployment in real-world scenarios. First, most methods operate at the instance level, failing to generalize to novel objects. Second, they heavily depend on prior information such as accurate 3D object models, object masks, or bounding boxes (Wen et al. 2024; Hu et al. 2019; Do et al. 2018), limiting their applicability. These limitations stem from their

*Equal contribution.

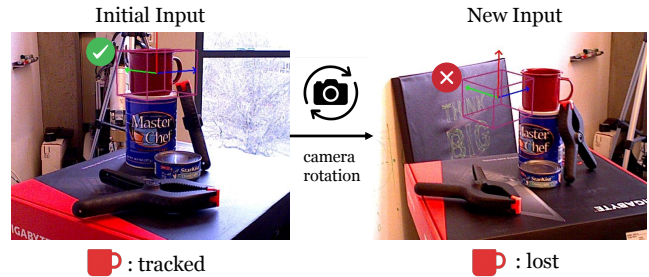


Figure 1: **Pose-estimation models lack robustness**, exemplified with FoundationPose (Wen et al. 2024), that fails to detect a mug under camera pose variation, highlighting its sensitivity to viewpoint shifts.

reliance on extensive reference information as model input, creating a bottleneck for practical deployment where systems must handle diverse, previously unseen objects.

Recent advances partially address these limitations through reference-based approaches and object-centric 3D reconstruction techniques.

CNOS (Nguyen et al. 2023) and PerSAM (Zhang et al. 2023) generate object masks in query frames by either rendering 3D models into reference images or using user-provided reference images. These methods employ pre-trained vision models (e.g., DINOv2 (Oquab et al. 2023)) to extract visual features and identify target objects through similarity matching. However, their performance degrades in cluttered scenes with occlusions due to their simplistic matching mechanism (e.g., cosine similarity). Moreover, they first segment all objects before performing individual comparisons, incurring substantial computational overhead. This makes it challenging to maintain object consistency across time.

Recent advances in object-centric 3D reconstruction further complement these reference-based methods. Classical approaches rely on multi-view stereo and RGB-D fusion or SLAM pipelines to build dense scene geometry (Dai et al., 2017; Engel, Schöps, and Cremers 2014), but typically operate at the scene level and require long, calibrated sequences. Neural 3D representations, such as object-centric radiance fields (Müller et al. 2022; Cerkez and Favaro 2024), learn

implicit 3D geometry and appearance directly from images and can generalize across object instances, yet they often demand careful optimization and multi-view coverage, limiting their practical use for real-time pose tracking.

These pose estimation limitations become particularly problematic in dynamic scenarios where objects move continuously. In real-world applications, agents both need to estimate poses at individual frames and to maintain consistent object identity across time. This naturally leads to the integration of tracking with pose estimation: while pose estimation provides precise per-frame spatial localization, tracking maintains temporal consistency across sequences—together enabling robust monitoring of object dynamics. Most existing tracking approaches rely on keypoint detection and template matching, often combined with particle filters to jointly estimate 3D translation and rotation (Wang et al. 2020; Wen et al. 2024; Deng et al. 2021). However, these methods suffer from major limitations: they tend to break down under heavy occlusion or object disappearance and, crucially, lack built-in mechanisms for detecting tracking failure. Figure 1 demonstrates the brittleness of current pose estimation models, exemplified with Foundation Pose (Wen et al. 2024), that fails to detect a mug after a camera rotation, revealing its fragility to viewpoint variation.

To address these challenges, we propose STORM (Segment, Track, and Object Re-localization from a single iMage), a unified framework for 6D object pose estimation that operates with minimal priors. Using only one or more reference images, STORM generates accurate object masks and recovers 6D poses, while performing object re-localization through a dedicated memory pool to enable reliable, continuous tracking. STORM comprises three key stages: First, we take one or more user-provided reference images of the target object and use a Large Language Model (LLM) to generate semantic descriptions compatible with CLIP (Radford et al. 2021). Based on these reference images, SAM3D is then employed to recover the 3D model of the object. Second, we extract spatial features from the reference and query images using visual encoders such as DINOv2. To bridge the domain gap between reference images and real-world imagery, we introduce Hierarchical Spatial Fusion Attention (HSFA)—a mechanism that fuses multi-view self-attention and cross-attention. Third, HSFA produces high-quality segmentation masks of the target object, which are combined with the reconstructed 3D model to estimate its 6D pose. To ensure robust tracking, we introduce a lightweight tracking-loss classifier that penalizes tracking failures using an efficient object memory mechanism. As a result, STORM automatically re-registers lost objects, achieving robust and reliable object tracking even under occlusion and rapid motion. Overall, we make the following contributions:

- We propose STORM, a unified framework for robust object pose estimation and tracking that requires one or multiple images of the target object to achieve accurate pose predictions.
- To enable robust segmentation and tracking, we intro-

duce Hierarchical Spatial Fusion Attention (HSFA) for fusing spatial and semantic features to produce high-quality masks, and design a novel tracking loss classifier that detects failures and enables automatic re-registration of potentially lost objects.

- We empirically demonstrate STORM’s effectiveness across multiple challenging benchmarks, achieving state-of-the-art performance in annotation-free 6D pose estimation and tracking.
- To evaluate the tracking robustness, we create a new dataset that represents object tracking as a classification task, by comparing the input image to a reference image. Our dataset covers diverse track-loss scenarios, including occlusion and rapid movement.

Let us now discuss the related work.

2 Background and Related Work

STORM is at the intersection of reference-based object segmentation, object-centric 3D reconstruction and object pose tracking.

Reference-based Object Segmentation. Early supervised methods like Mask R-CNN (He et al. 2017) achieve high accuracy but require expensive annotations and lack zero-shot capability. CLIPSeg (Lüddecke and Ecker 2022) enables text-prompted segmentation without instance data, yet produces coarse boundaries. Self-supervised approaches (e.g., UOAI-Net (Back et al. 2022)) and geometry-driven methods (e.g., SegICP (Wong et al. 2017)) struggle with occlusion and sensor noise, respectively. While SAM 2 (Ravi et al. 2024) generates high-recall proposals, it lacks instance association and requires post-processing. CNOS (Nguyen et al. 2023) refines SAM outputs using multi-view DINOv2 features (Oquab et al. 2023) for precise zero-shot segmentation, but suffers from high latency due to offline rendering. SAM-6D (Lin et al. 2024) combines SAM with geometric fitting but cannot achieve real-time performance. We propose the Segmenting Object Module (SOM) with Hierarchical Spatial Fusion Attention (HSFA) that fuses multi-view renderings and RGB features in real-time, producing high-precision masks without offline rendering, and incorporates failure detection for automatic re-registration.

Object-centric 3D Reconstruction. Traditional object-centric 3D reconstruction methods often rely on multi-view geometry and multi-view stereo techniques (Cremers and Kolev 2011), as well as large-scale scene-level reconstruction systems and datasets such as voxel-hashing-based real-time reconstruction (Nießner et al. 2013) and the ScanNet indoor reconstruction benchmark (Dai et al. 2017). These approaches typically require dense, calibrated multi-view imagery or pre-defined CAD models, leading to a trade-off between reconstruction quality, runtime, and deployment cost. More recent work explicitly focuses on object-centric 3D representation learning and reconstruction (Müller et al. 2022; Cerkezi and Favaro 2024), pushing object-level modeling toward more realistic and scalable scenarios. In contrast, STORM adopts SAM3D as its 3D reconstruction backend (Team et al. 2025), directly constructing object-level 3D

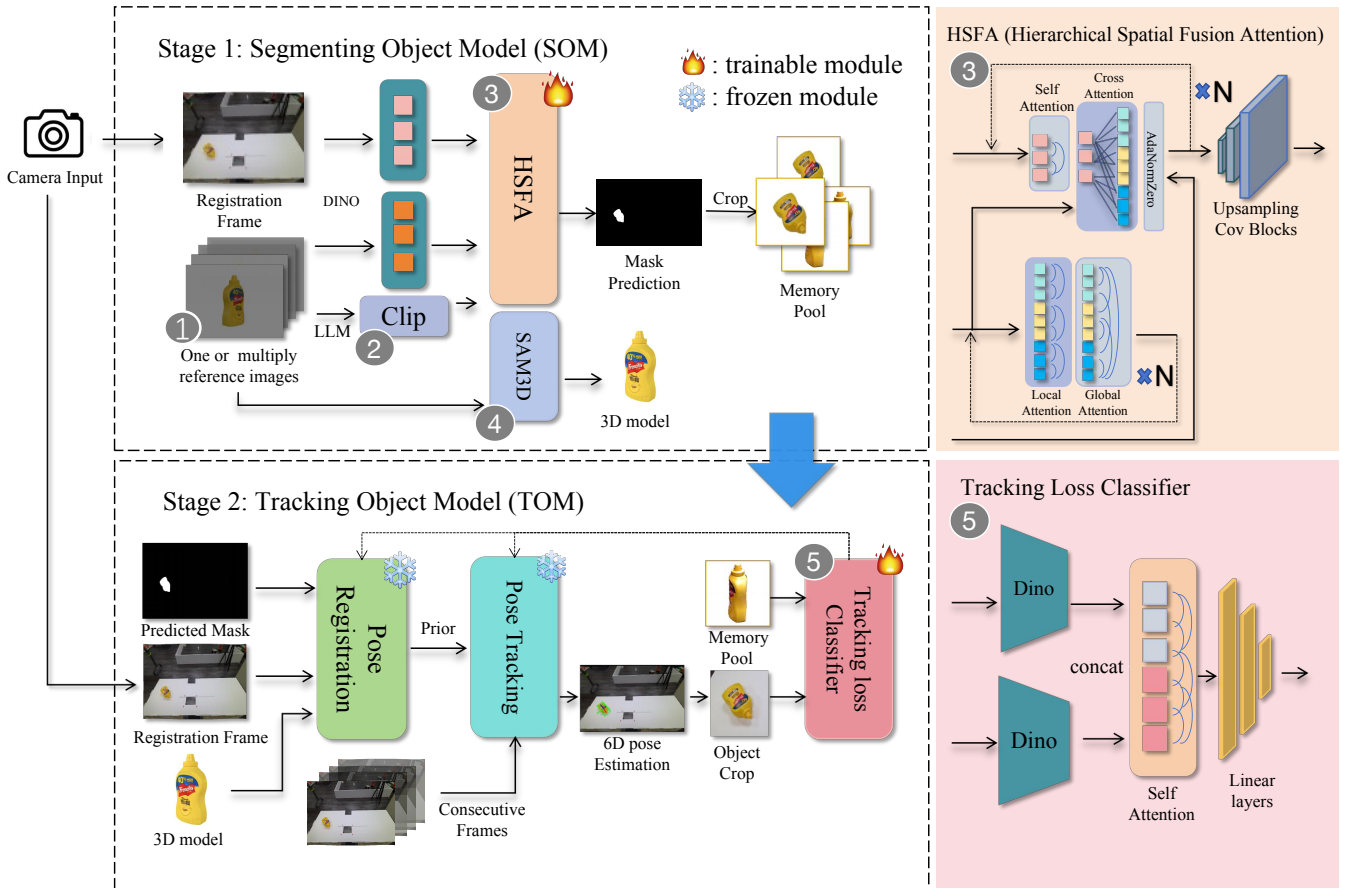


Figure 2: **Overview of STORM**, which is composed of two subsystems: the Segmenting Object Module (SOM) and the Tracking Object Module (TOM). SOM leverages reference images to generate a 3D model and, using their semantic and spatial information, integrates both intra-image and inter-image attention modules to capture spatial cues of the query frame through local and global attention blocks, producing a segmented mask. TOM classifies the output of the tracking module and utilizes the memory of SOM to perform re-registration when tracking fails, thereby ensuring robust and continuous tracking performance.

models from one or multiple reference images. Given reference RGB images and their corresponding segmentation masks, SAM3D produces high-fidelity 3D point clouds or meshes of the target object. This allows STORM to automatically obtain object-centric 3D models without manual CAD modeling or strong geometric priors, and to use these models as reliable input for downstream 6D pose estimation and tracking.

Object Pose Tracking. Current 6D pose trackers employ render-and-refine pipelines: an initial pose is iteratively refined by comparing rendered views against observations using methods like DeepIM (Li et al. 2018) or RBPF (Deng et al. 2021). FoundationPose (Wen et al. 2024) unifies various tracking paradigms under neural rendering, achieving state-of-the-art performance. However, these methods fail under occlusion, rapid motion, or view exits. Recovery strategies remain ad-hoc: DeepIM uses threshold-based re-initialization (Li et al. 2018), RBPF resets particles on weight-variance spikes (Deng et al. 2021), while others employ computationally expensive re-detection (Voigtlaender et al. 2020) or brittle histogram matching (Tjaden, Schwa-

necke, and Schomer 2017). We propose the Tracking Object Module (TOM), a lightweight failure detector that monitors tracking quality in real-time and triggers SOM-based segmentation and pose registration for rapid pose recovery, eliminating expensive rendering or two-stage detection.

3 STORM

We propose STORM, which addresses two key limitations of prior approaches: (i) the reliance on an initial object mask and 3D model for pose estimation, and (ii) the lack of mechanisms to recover from tracking failures. STORM leverages efficient, pre-established models for object segmentation, language understanding, 3D reconstruction, and pose estimation. As a result, it provides a fully automated pipeline: given one or multiple reference images, STORM localizes and segments the target object, infers its semantic attributes, builds its 3D model, estimates its 6D pose, and performs self-correcting tracking across frames. The inference process in STORM comprises two main components: the Segmenting Object Module (SOM) and the Tracking Ob-

ject Module (TOM). We now describe each component in detail.

Object Segmentation and 3D Model Generation from Reference Images

STORM robustly performs object segmentation by utilizing one or multiple provided reference images in conjunction with a novel attention-driven feature matching strategy.

Reference Images Preparation. As shown in Figure 2 ①, the reference images can be either a single or multiple clean images of the target object with a plain, single-color background, or a single or multiple masked reference images.

Semantic Prompt Generation. To acquire semantic information, we feed the reference images $I_{\text{reference}}$ and a short prompt p into a vision–language model (gemma-3n-E4B-it) (Team 2025), which produces a concise description of the object T (avoiding redundant information) and, by leveraging its prior knowledge, implicitly recovers a canonical, view-complete shape representation in the latent space. As depicted in Figure 2 ②, this textual description is then encoded by CLIP into a vector $e_t \in \mathbf{R}^d$, which, together with HSFA and image registration, aligns this latent shape with the observed views and establishes consistent point–pixel correspondences.

Rather than altering the backbone’s core features, we inject e_t into the downstream feature map $F \in \mathbf{R}^{H \times W \times C}$ by modifying its channel-wise normalization parameters. Specifically, we compute semantic offsets

$$\Delta\gamma = W_\gamma e_t, \quad \Delta\beta = W_\beta e_t,$$

applied to adjust each normalized feature as follows:

$$\hat{F}_{i,c} = (\gamma_c + \Delta\gamma_c) \frac{F_{i,c} - \mu_c}{\sigma_c + \varepsilon} + (\beta_c + \Delta\beta_c), \quad (1)$$

where μ_c is the mean activation of the channel c over all N patches, σ_c its standard deviation, and ε is a small constant (e.g. 10^{-9}) added for numerical stability. This subtle bias preserves the original per-patch representations while steering the network’s attention toward object-centric regions.

Feature Matching by Spatial Fusion. To bridge the distribution gap between reference images and real images and better capture the spatial information of the object, we introduce Hierarchical Spatial Fusion Attention (HSFA). As shown in Figure 2 ③, HSFA simultaneously leverages the feature representations of the real and reference frames, fusing their distinct contextual information to directly obtain high-quality mask predictions. Overall, HSFA processes the input as follows:

(1) *Capturing inter-view relationships and rich spatial representations.* Patch embeddings from each multi-view reference image are first processed independently using self-attention. These per-image embeddings are then concatenated across all views and passed through a joint local attention module, allowing the model to capture inter-view dependencies.

(2) *Extracting salient query representations.* The query frame’s patch embeddings are processed via self-attention. To preserve the original Dino features, HSFA performs the first round of cross-attention between the query embeddings and the *raw* multi-view embeddings (i.e., before spatial-attention refinement). In subsequent cross-attention layers, the query frame attends to the outputs of the previous spatial-attention block, promoting faster convergence and enhancing object salience.

(3) *Composing joint representations.* The Hierarchical Spatial Fusion Attention block integrates the query and multi-view embeddings, as described above. This fusion block is repeated n times to iteratively refine the joint features. Finally, an upsampling convolutional block generates the mask of the target object.

(4) *Injecting semantics.* To enrich object-level details and guide the attention mechanism toward the target, linguistic embeddings are injected into HSFA via the AdaNorm-Zero normalization scheme.

A detailed description of the full algorithm is provided in the Appendix. The output of the HSFA module is the segmentation mask of the target object: this mask is generated from a set of fused feature representations that jointly integrate spatial cues and contextual information from the query frame and the multi-view reference inputs. By progressively enhancing the responses of target-related regions during the hierarchical spatial fusion process, HSFA obtains a more accurate representation of the object’s shape and location, ultimately producing a high-quality target segmentation mask that can be directly used for subsequent pose estimation or tracking tasks.

3D Model Generation. As shown in Figure 2 ④, Given one or multiple reference images $\{I_{\text{ref}}^k\}$ of the target object, which can be either raw RGB images captured against a plain, single-color background or already masked images, we obtain the corresponding segmentation masks $\{M_{\text{ref}}^k\}$ either by simple background color thresholding or by directly reusing the provided masks, without any additional learning or manual annotation. We further apply a depth estimator to each reference view to obtain depth maps $\{D_{\text{ref}}^k\}$ and use them to align the reconstruction to the correct metric scale. The masked reference images and their depths are then fed into SAM3D to reconstruct a 3D model:

$$\mathcal{P}_{\text{ref}} = f_{\text{SAM3D}}(\{I_{\text{ref}}^k, M_{\text{ref}}^k, D_{\text{ref}}^k\}_k), \quad (2)$$

where \mathcal{P}_{ref} denotes the reconstructed, scale-consistent 3D point cloud (or mesh) of the target object. This reference 3D model is subsequently used for downstream 6D pose estimation and tracking.

Loss Optimization. STORM achieves high-quality segmentation by optimizing a joint loss function. To improve the precision of region predictions, we introduce a novel loss formulation that combines Tversky loss (Salehi, Erdogmus, and Gholipour 2017) with Focal loss (Lin et al. 2017):

$$\mathcal{L} = \sum_{i=1}^N [\lambda_T \ell_T(p_i, t_i) + \lambda_f \ell_{\text{focal}}(p_i, t_i)], \quad (3)$$

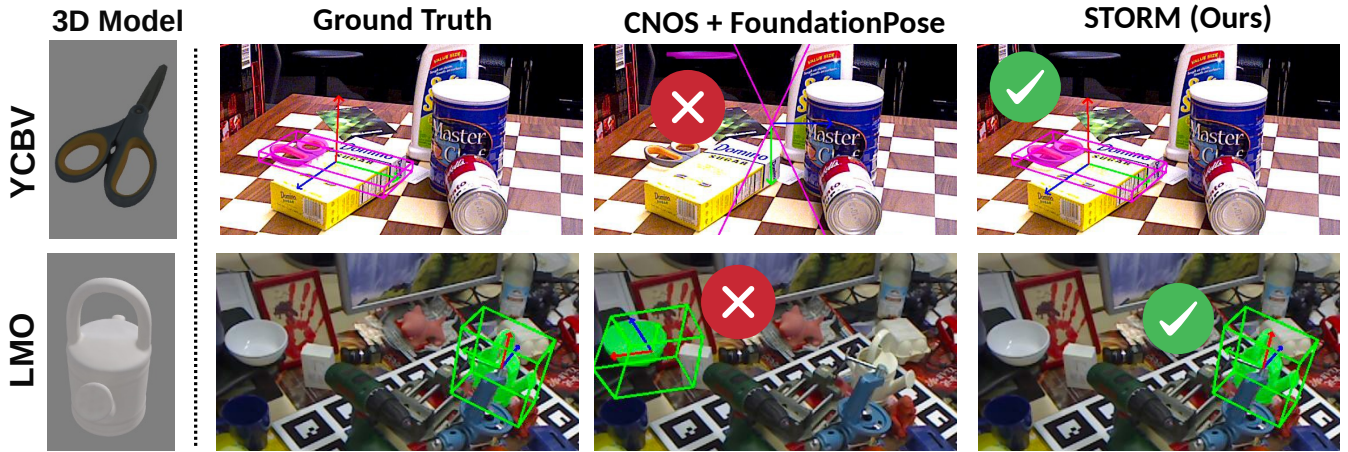


Figure 3: **STORM (SOM+TOM) achieves robust pose estimation for occluded objects in complex scenes.** We compare pose-estimation qualities on the LMO and YCB-V datasets, which comprise complex scenes with multiple and possibly occluded objects. As baselines, CNOS and GroundTruth are used to predict the segmentation mask, and FoundationPose was used to produce the pose estimation. The results indicate that our method produces pose estimates that are quantitatively and qualitatively close to the ground truth annotations in these scenarios. Detected objects are highlighted in green and pink.

where

$$\ell_T(p, t) = 1 - \frac{TP}{TP + \alpha FN + \beta FP}, \quad (4)$$

$$\ell_{\text{focal}}(p, t) = -(1-p)^\gamma t \ln p - p^\gamma (1-t) \ln(1-p),$$

where TP is the number of true-positive pixels of the region of interest, FN is the number of false-negative pixels, and FP is the number of false-positive pixels; $t \in \{0, 1\}$ is the ground-truth label for each pixel, and $p \in [0, 1]$ is the predicted probability that the pixel belongs to the region of interest. The hyperparameters are set as $\alpha = 0.3$, $\beta = 0.7$, $\gamma = 2.0$, $\lambda_T = 1.0$, and $\lambda_f = 0.2$. This loss formulation imposes a strong penalty on false positives, which not only effectively suppresses spurious predictions in background regions but also preserves finer discriminative ability along object boundaries. As a result, the model is able to produce compact, accurate, and detail-preserving high-quality segmentation masks that provide reliable region inputs for subsequent downstream tasks.

6D Pose Estimation and Robust Tracking

Conventional pose-estimation approaches leverage the object’s position in the previous frame as a *prior* for its tracking module. When the object moves rapidly, however, the difference between its positions in consecutive frames can become too large, causing the tracker to lose accuracy and ultimately fail. In cases of occlusion—when the object disappears from view—the tracker similarly loses the target. To address these challenges, STORM monitors tracking quality on a per-frame basis and automatically re-initializes the tracker whenever a failure is detected.

(1) *Initial Registration and Memory Construction.* For the first tracking frame, STORM uses its segmentation module to extract an object mask. This mask, along with the generated 3D model, is passed to the FoundationPose registration module to estimate the object’s 6D pose. At the

same time, a cropped RGB patch of the segmented object—referred to as a real crop—is stored in a memory pool. This crop serves as a visual reference for subsequent frames. In each new frame, the tracking module produces a pose estimate, which is compared to the memory pool to detect tracking failures. If the similarity falls below a threshold—due to rapid motion or occlusion—STORM flags the tracker as failed.

(2) *Re-initialization and Tracking Verification.* When a failure is detected, STORM automatically re-initializes the tracker by SOM to generate a new segmentation mask, then re-estimating the object’s pose. A new real crop from the current frame is also added to the memory pool, ensuring that visual references stay up to date. To enable robust and generalizable comparisons, As shown in Figure 2 (5), DINO is used as the feature-extraction backbone. Features from each frame are concatenated and passed through a lightweight tracking-verification subnetwork, which consists of a single self-attention layer followed by a fully connected layer and a sigmoid activation. This network outputs a binary score indicating whether tracking remains valid. The entire mechanism is designed for high efficiency, enabling real-time detection and recovery from tracking failures.

In the training phase, we optimize the network using the binary cross-entropy loss with logits (Rumelhart, Hinton, and Williams 1986), defined as

$$\mathcal{L} = -\frac{1}{N} \sum_{i=1}^N [y_i \log \sigma(z_i) + (1 - y_i) \log(1 - \sigma(z_i))], \quad (5)$$

with z_i the raw logit predicted for the i -th example, $\sigma(\cdot)$ the sigmoid function, and $y_i \in \{0, 1\}$ the ground-truth label.

Method	Mean ADD	Mean ADD-S	Mean AR
LM-O			
FP + CNOS	0.57	0.68	0.41
STORM (Ours)	0.74	0.89	0.53
FP + Ground Truth	0.78	0.93	0.56
YCB-Video			
FP + CNOS	0.73	0.92	0.69
STORM (Ours)	0.78	0.99	0.74
FP + Ground Truth	0.78	0.99	0.74

Table 1: **STORM improves annotation-free estimation.** ADD and ADD-S (Xiang et al. 2017) (*cf.* Appendix) and Average Recall (AR) on LM-O and YCB-Video. STORM approaches ground-truth performance and outperforms the prior annotation-free baseline (FoundationPose + CNOS).

4 Experimental evaluation

In our experiments, we evaluate the effectiveness of STORM in performing robust object segmentation, 6D pose estimation, and tracking in real time, while addressing key limitations of previous approaches. Specifically, we aim to answer the following research questions:

- Q1:** Can STORM automatically generate accurate 6D pose estimations in an end-to-end manner, without any manual intervention?
- Q2:** Can the segmentation module (SOM) produce high-quality object masks both accurately and efficiently?
- Q3:** Can the 3D models generated by SAM3D provide reliable, high-quality input for downstream 6D pose estimation?
- Q4:** Can the tracking module (TOM) reliably detect tracking failures and successfully perform re-localization and recovery of 6D pose?
- Q5:** How effective is the proposed tracking loss classifier with attention in detecting failures?

Let us now answer each research question step by step.

Fully Automatic 6D Pose Estimation

To answer **Q1**, we evaluate STORM on challenging industrial datasets for fully automated 6D pose estimation. We use established benchmarks—LM-O (Brachmann et al. 2014) and YCB-Video (Xiang et al. 2017)—that test pose estimation under realistic conditions. LM-O (LineMOD-Occluded) extends the original LineMOD dataset by introducing significant inter-object occlusion, allowing to test robustness in cluttered and occluded scenarios. YCB-Video provides real-world video sequences of household objects with accurate 6D pose annotations, ideal to evaluate pose estimation across time under varying viewpoints and lighting conditions.

We compare STORM against two baselines: (i) a DINO-based pipeline, which uses DINOv2 (Oquab et al. 2023) for feature extraction and point matching, followed by segmentation with SAM2, and (ii) a setup that uses ground-truth masks as input to FoundationPose. The DINO baseline represents a strong zero-shot segmentation approach,

while the ground-truth segmentation baseline provides an approximate upper bound for pose estimation performance. These comparisons highlight STORM’s ability to exceed state SOTA performances in an annotation-free manner.

We evaluated both datasets using standard metrics from the BOP benchmark: ADD, ADD-S (Xiang et al. 2017), and Average Recall (AR) (Hodàn et al. 2018). The ADD metric measures the average distance between corresponding 3D model points transformed by the predicted and ground-truth poses. ADD-S is a variant that handles pose ambiguities for objects that present symmetries by computing the distance to the nearest model point (*cf.* Appendix B for details).

Results. Figure 3 provides a qualitative comparison, visually confirming the accuracy of STORM’s predictions. Table 1 summarizes the quantitative results. On the LM-O dataset, STORM outperforms all baseline methods and achieves performance within just 4% of the variant that uses ground-truth masks. On the YCB-Video dataset, STORM matches the ground-truth setup exactly and exceeds the strong CNOS baseline by 5%. STORM produces pose estimations nearly indistinguishable from those obtained with manual annotations, underscoring its accuracy.

Segmentation Quality and Efficiency

To answer **Q2**, we evaluate the quality and the precision of the generated segmentation masks of the segmentation module (SOM) of STORM on several established benchmarks.

Our experiments are conducted on 5 core test datasets from the BOP benchmark suite (Hodaň et al. 2020): LM-O, T-LESS (Hodàn et al. 2017), TUD-Light (Hodàn et al. 2018), HomebrewedDB (Kaskman et al. 2019), and YCB-Video (Xiang et al. 2017). BOP (Benchmark for 6D Object Pose Estimation) is unified framework to evaluate pose estimation systems under consistent protocols with challenging conditions such as occlusion in the real-world scenario, symmetries, and background clutter. The selected benchmarks span 95 distinct objects types, encompassing textured and textureless objects, symmetric and asymmetric shapes, of both household and industrial items, providing a diverse testbed to test segmentation quality.

We compare STORM against the strongest publicly available systems on the BOP leaderboard. The baselines include ZebraPoseSAT-EffiNetB4 (Su et al. 2022) and Mask R-CNN (He et al. 2017), which are fine-tuned per object category, as well as NOCTIS, LDSEg, MUSE, Prisma-MPG-Complex, NIDS, SAM6D (Lin et al. 2024), CNOS, and ViewInvDet. Most baselines are distributed solely as executable packages via the BOP Challenge website without linked peer-reviewed publications, collectively referred to as the BOP Challenge Leaderboard¹. STORM is evaluated under the same protocol for a fair comparison.

We train the SOM model on the BOP-Classic-Core training set using rendered reference images from 16 uniformly sampled spherical viewpoints, enabling HSFA to learn object-centric correspondences from these renderings (see Appendix for complete training details).

¹<https://bop.felk.cvut.cz/challenges/>

mAP (\uparrow)	LM-O	T-LESS	TUD-L	HB	YCB-V	Mean	Time (s)
<i>Zero shot</i>							
STORM (SOM, Ours)	66.1	47.1	69.1	70.8	89.L3	68.5	0.183
NOCTIS	48.9	47.9	58.3	60.7	68.4	56.8	0.990
LDSeg	47.8	48.8	58.7	62.2	64.7	56.4	1.890
MUSE	47.8	45.1	56.5	59.7	67.2	55.3	0.559
NIDS	43.9	49.6	55.6	62.0	65.0	55.2	0.485
Prisma-MPG-Complex	46.0	45.8	58.4	59.6	61.0	54.2	1.276
SAM6D	46.0	45.1	56.9	59.3	60.5	53.6	2.795
ViewInvDet	41.0	38.5	46.4	54.5	61.6	48.4	1.700
CNOS (FastSAM)	39.7	37.4	48.0	51.1	59.9	47.2	0.221
CNOS (SAM)	39.6	39.7	39.1	48.0	59.5	45.2	1.847
<i>Supervised</i>							
ZebraPoseSAT-EffNetB4	51.6	72.1	71.8	68.9	73.1	67.5	0.080
Mask R-CNN	37.5	54.4	48.9	47.1	42.9	46.2	0.100

Table 2: **STORM (SOM) achieves high-quality and efficient segmentation.** Comparison of zero-shot and supervised segmentation methods on five BOP datasets. mAP scores are reported on LM-O, T-LESS, TUD-L, HB, and YCB-V. Zero-shot methods, including STORM (SOM), operate without any object-specific retraining, whereas supervised baselines are fine-tuned per object category. STORM (SOM) achieves the highest mean mAP while also being highly efficient in runtime. Best values are in bold, and \circ depicts the second best. SOM stands for the Segmenting Object Module in the STORM architecture.

Results. Table 2 presents a comparison of segmentation methods across the BOP datasets. ZebraPoseSAT-EffNetB4 achieves a mean Average Precision (mAP) (Lin et al. 2014) of 67.5%, making it the strongest baseline. Our segmentation module SOM achieves a higher mAP of 68.5%, with an average inference time of 0.183 seconds per image. Notably, SOM establishes a new state-of-the-art on four out of the five benchmarks—LM-O, T-LESS, HomebrewedDB, and YCB-Video—without any fine-tuning or retraining for specific object instances. These results highlight SOM’s strong generalization ability and efficiency.

Impact of 3D Model Quality on Pose Estimation

To answer **Q3**, we investigate whether the 3D models generated by SOM can serve as high-quality input for downstream 6D pose estimation. We evaluate STORM on the YCB-V dataset under two settings: using ground-truth 3D models as the baseline and using 3D models reconstructed from reference images as input to the downstream pose estimator. Figure 4 provides a qualitative comparison between the ground-truth CAD models and the aligned 3D models reconstructed from reference images using SAM3D. Across diverse object types, including bottles and cans, the SAM3D-generated models closely match the global geometry and fine-scale structure of the ground-truth models: object proportions, aspect ratios, and characteristic shape details (e.g., bottle necks, rims, and can lids) are faithfully preserved. Moreover, the reconstructed meshes often exhibit smoother and more regular contours along object boundaries, which can be beneficial for downstream pose estimation and rendering robustness. Only minor deviations in local surface detail and texture are observed, suggesting that SOM+SAM3D is capable of producing high-fidelity 3D geometry that is ef-

Method	VSD _{mean}	IoU _{mean}	ADD-S _{AUC}
SAM3D (unaligned) + FP	22.19	48.27	44.92
SAM3D (aligned) + FP	60.92	84.63	99.12
GT + FP	60.97	88.50	98.95

Table 3: **SAM3D-generated 3D models provide reliable input for pose estimation.** Mean pose metrics (VSD, IoU, ADD-S AUC) on YCB-V for SAM3D (unaligned) +Foundationpose, SAM3D (aligned) +Foundationpose, and GT+Foundationpose.

fectively indistinguishable from ground-truth CAD for the purposes of 6D pose estimation.

Results. As shown in Table 3, aligning the SAM3D-reconstructed models (SAM3D (aligned) + FP) improves pose accuracy over the unaligned variant (SAM3D (unaligned) + FP) and yields performance that is highly comparable to the ground-truth configuration (GT + FP), with only marginal differences in VSD, IoU, and ADD-S metrics. These results indicate that the 3D models produced by Aligned SAM3D are sufficiently accurate and reliable to serve as effective input for downstream 6D pose estimation.

Tracking Failure Detection and Recovery

To answer **Q4**, we evaluate whether STORM’s tracking module (TOM) can detect when it loses track of an object—that is, whether it exhibits self-awareness of tracking failure. To this end, we synthetically generate a dataset using BOP annotations, enabling TOM to learn to distinguish between successful and failed tracking by leveraging object



Figure 4: **Comparison of 3D models reconstructed from reference images and ground-truth 3D models.** The Aligned SAM3D models almost perfectly recover the underlying object structure while producing smoother and more regular contours along object boundaries.

Method	ADD	ADD-S	AR	Time(ms)
STORM (TOM)	74.64	88.56	67.85	98±5
FP Tracking	52.76	66.76	50.09	84±3

Table 4: **STORM(TOM) accurately detects tracking loss with minimal overhead.** Mean recall (ADD, ADD-S, AR) on YCB-Video for TOM and FoundationPose tracking.

crops, distractors, and viewpoint variations.

The training dataset is constructed using BOP as the source. For each object, we extract ground-truth masks to build a memory pool of clean object crops. Positive samples consist of segmented images and cropped images from the same object, serving as correctly tracked inputs for the classifier. Negative samples are generated in two ways: (i) pairing segmented images and crops from *different* objects to simulate object identity confusion; and (ii) simulating tracking drift by pairing the segmented images with either randomly shifted crop regions around the mask or randomly cropped image regions. This carefully designed training strategy enables TOM to learn subtle visual cues distinguishing successful tracking from failure cases.

Moreover, to evaluate TOM’s ability to detect tracking loss under challenging conditions such as rapid motion and occlusion, we use the YCB-Video dataset with the following modifications. We simulate high-speed object motion by dropping the video frames randomly and simulate occlusion by applying random masks over the object regions.

Results. Table 4 shows the tracking performance when evaluating on the modified YCB-V dataset. Our method significantly outperforms the baseline without tracking-loss detection, while adding only 13ms of inference overhead—demonstrating both accuracy and efficiency. This result reinforces a core insight of our framework: once tracking loss occurs, the resulting drift is often irrecoverable with traditional tracking methods, especially at longer sampling intervals. Figure 5 further demonstrates STORM’s robustness in object tracking. Due to camera rotation, both STORM and FoundationPose lost the target object being tracked. However, STORM automatically detected the tracking failure and successfully recovered, while FoundationPose failed to re-track due to the absence of a tracking fail-

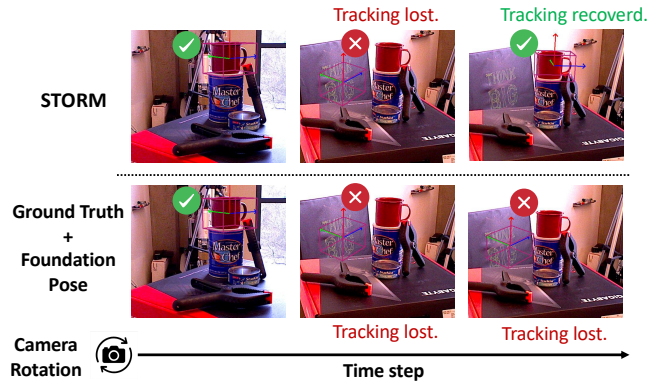


Figure 5: **STORM automatically recovers from tracking failures.** A demonstration of the Tracking Object Module (TOM) successfully re-tracking a lost object. In contrast, FoundationPose fails to recover once tracking is lost.

Models	Accuracy (%)	Time (ms)
Cosine Similarity	87.55	12.4
TOM (w/o Attention)	95.23	12.2
TOM (Attention, 1 layer)	98.36	13.5
TOM (Attention, 2 layer)	97.84	16.8

Table 5: **STORM gains performance by attention-based matching.** Accuracy and inference time with different configurations on the tracking dataset.

ure detection mechanism. These results validate the effectiveness of STORM’s tracking module in maintaining robust object tracking under challenging conditions.

Tracking Loss Classification with Attention

To answer Q5, we compare the performances of different matching strategies on the tracking-loss classification task. Using our tracking dataset, we compare STORM’s tracking module (TOM) with different configurations against a simple cosine similarity baseline. Table 5 provides the accuracy and inference time. Adding a single attention layer significantly improves accuracy from 87.55% (cosine similarity) to 98.36%, with only 1.3ms of additional latency per frame. The model without attention already achieves detection accuracy of 95.23% while maintaining the fastest inference at 12.2ms. Adding a second attention layer does not improve the accuracy but increasing latency to 16.8ms, indicating that a single attention layer optimally balances accuracy and latency. TOM’s attention mechanism is crucial for robust tracking failure detection, substantially outperforming simple feature matching approaches while maintaining inference time suitable for real-time applications.

5 Conclusion

To conclude, we introduced STORM, an automatic, annotation-free framework for 6D object pose estimation and tracking that operates purely from one or a few reference images, without requiring any pre-defined 3D models.

STORM integrates a supervision-free segmentation module with a robust tracking component, and employs an attention-based feature fusion mechanism to jointly process input and reference images. We further reformulate tracking as a classification task for detecting tracking failures.

In our experiments, STORM achieves strong detection and pose estimation performance across multiple standard benchmarks, significantly outperforming prior methods and even surpassing state-of-the-art baselines, while incurring minimal computational overhead. Future work will extend STORM to multi-object and category-level tracking, incorporate multi-modal depth sensing, and explore relational reasoning (Shindo et al. 2024) and large-scale semantic prompting to support more complex manipulation tasks.

References

- Back, S.; Lee, J.; Kim, T.; Noh, S.; Kang, R.; Bak, S.; and Lee, K. 2022. Unseen object amodal instance segmentation via hierarchical occlusion modeling. In *International Conference on Robotics and Automation (ICRA)*.
- Brachmann, E.; Krull, A.; Michel, F.; Gumhold, S.; Shotton, J.; and Rother, C. 2014. Learning 6d object pose estimation using 3d object coordinates. In *ECCV 2014: 13th European Conference*.
- Cerkezci, L.; and Favaro, P. 2024. Sparse 3D Reconstruction via Object-Centric Ray Sampling. In *Proceedings of the International Conference on 3D Vision (3DV)*.
- Cremers, D.; and Kolev, K. 2011. Multiview Stereo and Silhouette Consistency via Convex Functionals over Convex Domains. *IEEE Transactions on Pattern Analysis and Machine Intelligence*, 33(6): 1161–1174.
- Dai, A.; Chang, A. X.; Savva, M.; Halber, M.; Funkhouser, T.; and Nießner, M. 2017. ScanNet: Richly-Annotated 3D Reconstructions of Indoor Scenes. In *Proceedings of the IEEE Conference on Computer Vision and Pattern Recognition (CVPR)*, 5828–5839.
- Dai, A.; Nießner, M.; Zollhöfer, M.; Izadi, S.; and Theobalt, C. 2021. BundlEfusion: Real-time globally consistent 3d reconstruction using on-the-fly surface reintegration. *ACM Transactions on Graphics (ToG)*.
- Deng, X.; Mousavian, A.; Xiang, Y.; Xia, F.; Bretl, T.; and Fox, D. 2021. PoseRBPF: A Rao–Blackwellized particle filter for 6-D object pose tracking. *IEEE Transactions on Robotics*.
- Do, T.-T.; Cai, M.; Pham, T.; and Reid, I. 2018. Deep6dpose: Recovering 6d object pose from a single rgb image. *arXiv preprint*.
- Engel, J.; Schöps, T.; and Cremers, D. 2014. LSD-SLAM: Large-scale Direct Monocular SLAM. In *Computer Vision – ECCV 2014*, volume 8690 of *Lecture Notes in Computer Science*, 834–849. Springer.
- He, K.; Gkioxari, G.; Dollár, P.; and Girshick, R. 2017. Mask R-CNN. In *IEEE International Conference on Computer Vision (ICCV)*.
- He, Y.; Huang, H.; Fan, H.; Chen, Q.; and Sun, J. 2021. Ffb6d: A full flow bidirectional fusion network for 6d pose estimation. In *Proceedings of the IEEE/CVF conference on computer vision and pattern recognition*.
- He, Y.; Sun, W.; Huang, H.; Liu, J.; Fan, H.; and Sun, J. 2020. Pvn3d: A deep point-wise 3d keypoints voting network for 6dof pose estimation. In *Proceedings of the IEEE/CVF conference on computer vision and pattern recognition*.
- Hinterstoisser, S.; Lepetit, V.; Ilic, S.; Holzer, S.; Bradski, G.; Konolige, K.; and Navab, N. 2012. Model based training, detection and pose estimation of texture-less 3d objects in heavily cluttered scenes. In *Asian conference on computer vision*.
- Hodan, T.; Haluza, P.; Obdržálek, Š.; Matas, J.; Lourakis, M.; and Zabulis, X. 2017. T-LESS: An RGB-D Dataset for 6D Pose Estimation of Texture-less Objects. In *IEEE Winter Conference on Applications of Computer Vision (WACV)*.
- Hodan, T.; Michel, F.; Brachmann, E.; Kehl, W.; Glent Buch, A.; Kraft, D.; Drost, B.; Vidal, J.; Ihrke, S.; Zabulis, X.; Sahin, C.; Manhardt, F.; Tombari, F.; Kim, T.; Matas, J.; and Rother, C. 2018. BOP: Benchmark for 6D Object Pose Estimation. In *European Conference on Computer Vision (ECCV)*.
- Hodaň, T.; Sundermeyer, M.; Drost, B.; Labbé, Y.; Brachmann, E.; Michel, F.; Rother, C.; and Matas, J. 2020. BOP challenge 2020 on 6D object localization. In *ECCV 2020 Workshops*.
- Hu, Y.; Hugonot, J.; Fua, P.; and Salzmann, M. 2019. Segmentation-driven 6d object pose estimation. In *Proceedings of the IEEE/CVF conference on computer vision and pattern recognition*, 3385–3394.
- Kappler, D.; Meier, F.; Issac, J.; Mainprice, J.; Cifuentes, C. G.; Wüthrich, M.; Berenz, V.; Schaal, S.; Ratliff, N.; and Bohg, J. 2018. Real-time perception meets reactive motion generation. *IEEE Robotics and Automation Letters*.
- Kaskman, R.; Zakharov, S.; Shugurov, I.; and Ilic, S. 2019. HomebrewedDB: RGB-D Dataset for 6D Pose Estimation of 3D Objects. In *IEEE/CVF International Conference on Computer Vision Workshops (ICCVW)*.
- Labbé, Y.; Carpentier, J.; Aubry, M.; and Sivic, J. 2020. Cosypose: Consistent multi-view multi-object 6d pose estimation. In *ECCV 2020: 16th European Conference*. Springer.
- Li, Y.; Wang, G.; Ji, X.; Xiang, Y.; and Fox, D. 2018. Deepim: Deep iterative matching for 6d pose estimation. In *Proceedings of the European conference on computer vision (ECCV)*.
- Lin, J.; Liu, L.; Lu, D.; and Jia, K. 2024. Sam-6d: Segment anything model meets zero-shot 6d object pose estimation. In *Conference on Computer Vision and Pattern Recognition*.
- Lin, T.-Y.; Goyal, P.; Girshick, R.; He, K.; and Dollár, P. 2017. Focal loss for dense object detection. In *Proceedings of the IEEE international conference on computer vision*.
- Lin, T.-Y.; Maire, M.; Belongie, S.; Hays, J.; Perona, P.; Ramanan, D.; Dollár, P.; and Zitnick, C. L. 2014. Microsoft coco: Common objects in context. In *European conference on computer vision*.
- Loshchilov, I.; and Hutter, F. 2016. Sgdr: Stochastic gradient descent with warm restarts. *arXiv preprint*.
- Lüddecke, T.; and Ecker, A. 2022. Image segmentation using text and image prompts. In *Proceedings of the IEEE/CVF conference on computer vision and pattern recognition*.
- Marchand, E.; Uchiyama, H.; and Spindler, F. 2015. Pose estimation for augmented reality: a hands-on survey. *IEEE transactions on visualization and computer graphics*.
- Müller, N.; Simonelli, A.; Porzi, L.; Rota Bulò, S.; Nießner, M.; and Kotschieder, P. 2022. AutoRF: Learning 3D Object Radiance Fields from Single View Observations. In *Proceedings of the IEEE/CVF Conference on Computer Vision and Pattern Recognition (CVPR)*, 3961–3970.
- Nguyen, V. N.; Groueix, T.; Ponimatkin, G.; Lepetit, V.; and Hodan, T. 2023. Cnos: A strong baseline for cad-based novel

- object segmentation. In *Proceedings of the IEEE/CVF International Conference on Computer Vision*.
- Nießner, M.; Zollhöfer, M.; Izadi, S.; and Stamminger, M. 2013. Real-time 3D Reconstruction at Scale using Voxel Hashing. *ACM Transactions on Graphics*, 32(6): 169:1–169:11.
- Oquab, M.; Darcet, T.; Moutakanni, T.; Vo, H.; Szafraniec, M.; Khalidov, V.; Fernandez, P.; Haziza, D.; Massa, F.; El-Nouby, A.; et al. 2023. Dinov2: Learning robust visual features without supervision. *arXiv preprint*.
- Park, K.; Patten, T.; and Vincze, M. 2019. Pix2pose: Pixel-wise coordinate regression of objects for 6d pose estimation. In *Proceedings of the IEEE/CVF international conference on computer vision*.
- Pascanu, R.; Mikolov, T.; and Bengio, Y. 2013. On the difficulty of training recurrent neural networks. In *Proceedings of the 30th International Conference on Machine Learning*.
- Radford, A.; Kim, J. W.; Hallacy, C.; Ramesh, A.; Goh, G.; Agarwal, S.; Sastry, G.; Askell, A.; Mishkin, P.; Clark, J.; et al. 2021. Learning transferable visual models from natural language supervision. In *International conference on machine learning*.
- Ravi, N.; Gabeur, V.; Hu, Y.-T.; Hu, R.; Ryali, C.; Ma, T.; Khedr, H.; Rädle, R.; Rolland, C.; Gustafson, L.; et al. 2024. Sam 2: Segment anything in images and videos. *arXiv preprint*.
- Rennie, C.; Shome, R.; Bekris, K. E.; and De Souza, A. F. 2016. A dataset for improved rgb-d based object detection and pose estimation for warehouse pick-and-place. *IEEE Robotics and Automation Letters*.
- Rumelhart, D. E.; Hinton, G. E.; and Williams, R. J. 1986. Learning representations by back-propagating errors. *nature*.
- Salehi, S. S. M.; Erdogmus, D.; and Gholipour, A. 2017. Tversky loss function for image segmentation using 3D fully convolutional deep networks. In *International workshop on machine learning in medical imaging*.
- Shindo, H.; Brack, M.; Sudhakaran, G.; Dhami, D. S.; Schramowski, P.; and Kersting, K. 2024. Deisam: Segment anything with deictic prompting. *Advances in Neural Information Processing Systems*.
- Su, Y.; Saleh, M.; Fetzer, T.; Rambach, J.; Navab, N.; Busam, B.; Stricker, D.; and Tombari, F. 2022. Zebrapose: Coarse to fine surface encoding for 6dof object pose estimation. In *Proceedings of the IEEE/CVF Conference on Computer Vision and Pattern Recognition*.
- Team, G. 2025. Gemma 3n.
- Team, S. D.; Chen, X.; Chu, F.-J.; Gleize, P.; Liang, K. J.; Sax, A.; Tang, H.; Wang, W.; Guo, M.; Hardin, T.; Li, X.; Lin, A.; Liu, J.; Ma, Z.; Sagar, A.; Song, B.; Wang, X.; Yang, J.; Zhang, B.; Dollár, P.; Gkioxari, G.; Feiszli, M.; and Malik, J. 2025. SAM 3D: 3Dfy Anything in Images.
- Tjaden, H.; Schwanecke, U.; and Schomer, E. 2017. Real-time monocular pose estimation of 3D objects using temporally consistent local color histograms. In *Proceedings of the IEEE international conference on computer vision*.
- Voigtlaender, P.; Luiten, J.; Torr, P. H.; and Leibe, B. 2020. Siam r-cnn: Visual tracking by re-detection. In *Proceedings of the IEEE/CVF conference on computer vision and pattern recognition*.
- Wang, C.; Martín-Martín, R.; Xu, D.; Lv, J.; Lu, C.; Fei-Fei, L.; Savarese, S.; and Zhu, Y. 2020. 6-pack: Category-level 6d pose tracker with anchor-based keypoints. In *2020 IEEE International Conference on Robotics and Automation (ICRA)*.
- Wen, B.; Lian, W.; Bekris, K.; and Schaal, S. 2022. You only demonstrate once: Category-level manipulation from single visual demonstration. *arXiv preprint*.
- Wen, B.; Mitash, C.; Soorian, S.; Kimmel, A.; Sintov, A.; and Bekris, K. E. 2020. Robust, occlusion-aware pose estimation for objects grasped by adaptive hands. In *2020 IEEE International Conference on Robotics and Automation (ICRA)*.
- Wen, B.; Yang, W.; Kautz, J.; and Birchfield, S. 2024. Foundationpose: Unified 6d pose estimation and tracking of novel objects. In *Proceedings of the IEEE/CVF Conference on Computer Vision and Pattern Recognition*.
- Wong, J. M.; Kee, V.; Le, T.; Wagner, S.; Mariottini, G.-L.; Schneider, A.; Hamilton, L.; Chipalkatty, R.; Hebert, M.; Johnson, D. M.; et al. 2017. Segicp: Integrated deep semantic segmentation and pose estimation. In *International Conference on Intelligent Robots and Systems (IROS)*.
- Xiang, Y.; Schmidt, T.; Narayanan, V.; and Fox, D. 2017. Posecnn: A convolutional neural network for 6d object pose estimation in cluttered scenes. *arXiv preprint*.
- Zhang, R.; Jiang, Z.; Guo, Z.; Yan, S.; Pan, J.; Ma, X.; Dong, H.; Gao, P.; and Li, H. 2023. Personalize segment anything model with one shot. In *The Twelfth International Conference on Learning Representations*.

A HSFA Algorithm

Algorithm 1 outlines our proposed HSFA mechanism, designed to integrate multimodal features and exploit spatial interactions across query and reference views in a structured, iterative fashion. At the core of the algorithm lies a multi-stage attention pipeline operating over n iterative fusion steps.

In each iteration, the query features E^q are first updated via a self-attention mechanism to enhance internal dependencies and contextual coherence within the query representation (Line 2). These updated features are then fused with the reference features E^{ref} using cross-attention, enabling the query to extract relevant information from the reference context (Line 4). To inject multimodal cues, text embeddings E^t are incorporated into the query stream via residual addition followed by layer normalization (Line 6).

Next, the algorithm processes the reference features by first decomposing the concatenated E^{ref} into a set of m individual reference features E_1^r, \dots, E_m^r , each corresponding to a separate reference image (Line 8). Each of these reference feature maps is independently refined via self-attention (Line 10), capturing local spatial patterns within each view. The updated features are then reassembled into a single tensor (Line 12) and subjected to a final round of global self-attention (Line 14), modeling inter-image relations across the entire reference set.

After n fusion iterations, the refined query representation is passed through an upsampling convolutional block to generate a high-resolution prediction (Line 17). This final output, denoted as H , forms the region of interest prediction with enhanced spatial and multimodal coherence.

B Metric Details

ADD (Average Distance of Model Points)

The ADD metric measures the average Euclidean distance between the 3D model points transformed by the predicted pose and those transformed by the ground-truth pose. It is defined as:

$$\text{ADD} = \frac{1}{|M|} \sum_{x \in M} \|(Rx + t) - (R_{\text{gt}}x + t_{\text{gt}})\|, \quad (6)$$

where M is the set of 3D model points, (R, t) is the estimated rotation and translation, and $(R_{\text{gt}}, t_{\text{gt}})$ is the ground-truth pose. A prediction is considered correct if the ADD score is below a certain threshold, typically set to 10% of the object’s diameter.

ADD-S (Average Distance for Symmetric Objects)

For symmetric objects, the ADD-S metric is used to account for pose ambiguity. Instead of comparing each model point to its exact correspondence, ADD-S computes the distance to the nearest model point under the predicted and ground-truth poses:

$$\text{ADD-S} = \frac{1}{|M|} \sum_{x_1 \in M} \min_{x_2 \in M} \|(Rx_1 + t) - (R_{\text{gt}}x_2 + t_{\text{gt}})\|. \quad (7)$$

Algorithm 1: Hierarchic Spatial Fusion Attention

```

1: for  $j = 1$  to  $n$  do
2:    $E^q \leftarrow \text{SelfAttention}(E^q)$ 
3:   ## Apply self-attention on query features to capture internal dependencies
4:    $E^q \leftarrow \text{CrossAttention}(E^q, E^{\text{ref}})$ 
5:   ## Fuse query and reference features via cross-attention
6:    $E^q \leftarrow \text{AddNormZero}(E^q, E^t)$ 
7:   ## Add text features to query features followed by normalization to incorporate multimodal information
8:    $\{E_1^r, \dots, E_m^r\} \leftarrow \text{Split}(E^{\text{ref}})$ 
9:   ## Split the concatenated reference features back into individual image features
10:  for  $i = 1$  to  $m$  do
11:     $E_i^r \leftarrow \text{SelfAttention}(E_i^r)$ 
12:    ## Update each reference image feature independently with self-attention
13:  end for
14:   $E^{\text{ref}} \leftarrow \text{Concat}(E_1^r, \dots, E_m^r)$ 
15:  ## Re-concatenate the updated reference features
16:   $E^{\text{ref}} \leftarrow \text{SelfAttention}(E^{\text{ref}})$ 
17:  ## Apply self-attention on the concatenated reference features to model global interactions
18: end for
19:  $H \leftarrow \text{UpsampleConvBlock}(E^q)$ 
20: ## Upsample and refine query features through an upsampling convolutional block
21: ## Return the final high-resolution region of interest

```

This formulation handles symmetrical cases (e.g., cylindrical or handle-less objects) where multiple poses result in the same visual appearance.

Interpretation In both metrics, lower values indicate better pose alignment. ADD is suitable for asymmetric objects, while ADD-S is essential for evaluating symmetric ones. These metrics are widely adopted in benchmarks such as BOP for assessing the accuracy of 6D object pose estimation methods.

mAP(mean Average Precision)

For BOP dataset evaluation, we exclude all test samples with visibility lower than 0.1 and evaluate it by mAP, the overall score is computed in three stages.

Per-category AP Define the set of IoU thresholds

$$T = \{0.50, 0.55, \dots, 0.95\}. \quad (8)$$

For each category c ,

$$\text{AP}_c = \frac{1}{|T|} \sum_{t \in T} \text{Precision}_c(\text{IoU} = t). \quad (9)$$

Only instances with visible area $\geq 10\%$ are counted; smaller ones are ignored.

Dataset-level mean AP For each dataset d with category set \mathcal{C}_d ,

$$AP_d = \frac{1}{|\mathcal{C}_d|} \sum_{c \in \mathcal{C}_d} AP_c. \quad (10)$$

At evaluation time, only the top-100 predictions per image are kept.

Overall mAP Let the core datasets be \mathcal{D} .

$$mAP = \frac{1}{|\mathcal{D}|} \sum_{d \in \mathcal{D}} AP_d. \quad (11)$$

AR(Average Recall)

Per-error-function Average Recall An estimated pose is correct w.r.t. error function e if $e < \theta_e$. Define the set of thresholds Θ_e (and misalignment tolerances τ for VSD):

$$AR_e = \frac{1}{|\Theta_e|} \sum_{(\theta, \tau) \in \Theta_e} \text{Recall}_e(\theta, \tau). \quad (12)$$

Dataset-level Average Recall For dataset d ,

$$AR_d = \frac{1}{3} (AR_{VSD} + AR_{MSSD} + AR_{MSPD}). \quad (13)$$

Overall Average Recall. Let the core datasets be \mathcal{D} . Then

$$AR_C = \frac{1}{|\mathcal{D}|} \sum_{d \in \mathcal{D}} AR_d. \quad (14)$$

C Experimental Details

Hardware Information

All experiments are conducted on a server equipped with an AMD EPYC 7343 16-Core Processor (2.0–3.2 GHz, 64 threads), 500 GB of DDR4 RAM with an additional 8 GB swap space, and an NVIDIA RTX A6000 GPU with 48 GB of GDDR6 memory.

Q2 Training Details

To ensure that the proposed method remains entirely label-free, we rely exclusively on unlabeled RGB frames. Specifically, we trained the SOM model on a combined subset of the LMO, LM (Hinterstoisser et al. 2012), YCBV, HB, TLESS, TUDL, TYOL (Hodàn et al. 2018), and RU-APC (Rennie et al. 2016) datasets using eight A100 GPUs. To enhance the robustness of our model, we performed data augmentation via different lighting transformations and random rotations and translations. The learning rate scheduling strategy employed involved a warm-up phase followed by cosine annealing (Loshchilov and Hutter 2016), complemented by gradient clipping (Pascanu, Mikolov, and Bengio 2013) to mitigate individual factors potentially causing training instability. Additionally, we utilized a frozen encoder from Dinov2’s register to extract clean feature maps for training. The test set was drawn from the BOP Challenge test set. During training, no class labels or pose annotations were utilized. Instead, we created a reference image set by rendering the provided 3D model images from 16 uniformly

sampled spherical viewpoints. Subsequently, HSFA was applied to align features from these reference views and facilitate interaction with query views, effectively suppressing activations in background regions. This approach enabled the model to learn object-centric correspondences without any human supervision.

D Implementation Details

Implementation of SOM

Data Augmentation During training, each query image and its corresponding mask are subjected to joint photometric and geometric transforms. Specifically:

Photometric Augmentation. We apply ColorJitter with brightness variation of $\pm 30\%$, contrast variation of $\pm 30\%$, saturation variation of $\pm 30\%$, and hue adjustment of ± 0.1 .

Geometric Augmentation. A horizontal flip is performed with probability 0.5, synchronized between the image and its mask. In addition, a random affine transform is applied with rotation uniformly sampled from $[-180^\circ, +180^\circ]$, scale sampled from $[0.95, 1.05]$, and shear sampled from $[-25^\circ, +25^\circ]$; bicubic interpolation is used for images, while nearest-neighbor interpolation is used for masks.

Resize & Crop. All outputs are first resized so that the shorter edge matches the target length (using bicubic interpolation for images and nearest-neighbor for masks), then center-cropped to a spatial size of $H \times W$.

Tensor Conversion & Normalization. Images are converted to tensors and normalized using ImageNet statistics $\mu = [0.485, 0.456, 0.406]$ and $\sigma = [0.229, 0.224, 0.225]$; masks are converted to single-channel tensors without further normalization.

Random Erasing. With probability $p = 0.5$, we erase a random rectangle covering 2–10% of the image area (aspect ratio between 0.3 and 3.3), filling it with random pixel values in the image and zeros in the mask.

Training Details

Optimization & Learning Rate Schedule. We use SGD with an initial learning rate $\eta_0 = 0.01$ and no weight decay. The learning rate schedule consists of a linear warm-up followed by cosine annealing over a total of $T = 80,000$ steps:

$$\eta(t) = \begin{cases} \eta_0 \frac{t}{5,000}, & 0 \leq t < 5,000, \\ \frac{1}{2} \eta_0 \left(1 + \cos\left(\frac{(t-5,000)\pi}{T-5,000}\right) \right), & 5,000 \leq t \leq 80,000. \end{cases}$$

Loss Function Hyperparameters.

Focal Loss. The weight is set to $w_{\text{Focal}} = 20.0$, with hyperparameters $\alpha = 0.25$ and $\gamma = 2.0$.

Dice Loss. The weight is set to $w_{\text{Dice}} = 1.0$.

IoU Loss. The weight is set to $w_{\text{IoU}} = 1.0$.

Tversky Loss. The weight is set to $w_{\text{Tversky}} = 0.2$, with hyperparameters $\alpha = 0.5$ and $\beta = 0.5$.

Gradient Clipping. To stabilize training, we apply gradient-norm clipping after each backward pass:

$$\text{clip_grad_norm}(\nabla\theta, \text{max_norm} = 0.1).$$

This ensures the total norm of gradients does not exceed 0.1.

Implementation of TOM

Dataset Cf. Appendix F.

Training Details The training is carried out on an NVIDIA A6000 GPU with a batch size of 64, optimizing the model via the Adam algorithm at a learning rate of 1×10^{-4} and measuring error with binary cross-entropy with logits (BCEWithLogitsLoss). The training runs for 10 epochs.

The binary cross-entropy with logits loss is defined as:

$$\mathcal{L}(\mathbf{z}, \mathbf{y}) = \frac{1}{N} \sum_{i=1}^N \left[\max(z_i, 0) - z_i y_i + \log(1 + e^{-|z_i|}) \right], \quad (15)$$

where z_i is the model’s logit output, $y_i \in \{0, 1\}$ the target label, and N the batch size.

The Adam parameter update at iteration t follows:

$$\begin{aligned} m_t &= \beta_1 m_{t-1} + (1 - \beta_1) g_t, \\ v_t &= \beta_2 v_{t-1} + (1 - \beta_2) g_t^2, \\ \hat{m}_t &= \frac{m_t}{1 - \beta_1^t}, \quad \hat{v}_t = \frac{v_t}{1 - \beta_2^t}, \\ \theta_{t+1} &= \theta_t - \eta \frac{\hat{m}_t}{\sqrt{\hat{v}_t + \epsilon}}, \end{aligned} \quad (16)$$

where g_t is the gradient, β_1, β_2 are decay rates, η is the learning rate, and ϵ a stability term.

E Ablation Details

Settings. To validate the effectiveness of SOM, we conducted the following experiments. All training was performed on eight A100 GPUs. Except for disabling all data augmentation, the remaining settings were consistent with those described in Appendix D. We evaluated the loss convergence and the speed of loss reduction, as well as the Precision or AP metrics on the test dataset after every 1000 steps. Additionally, we examined the impact of language injection and the effects of using different HSFA layers.

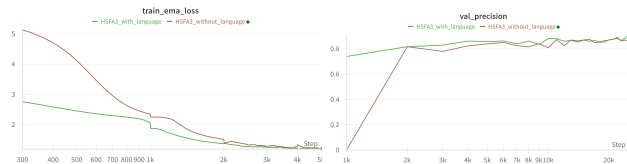


Figure 6: Under the same experimental conditions, we compared the convergence behavior of the training EMA loss and the prediction precision in test datasets for the HSFA3 layer, with and without language injection.

Ablation on Language Injection of SOM We compared models with and without language embedding. As depicted in Fig.6, the model with language embedding already

achieves favorable initialization in both loss and precision, and demonstrates faster convergence as well as better results after 10,000 steps compared to the model without language embedding. This confirms the effectiveness of our AdaNorm Zero-based language embedding design. Detailed quantitative results can be found in Table6, which shows that semantic guidance through language injection increases the average AP from 0.86 to 0.91, although inference time also increases from 0.196 seconds to 0.265 seconds. These results verify that language prompts can indeed improve localization quality, albeit at the cost of increased computational load per image due to the need for a large model to generate language descriptions.

Configuration	Average AP	Time (s)
SOM Without Language	0.87	0.196
SOM With Language	0.91	0.265

Table 6: Impact of language embedding on detection accuracy (AP) on datasets of Bop Challenge and inference speed.

Ablation on HSFA module in SOM As shown in Fig. 7, we compared the training loss, EMA loss, and AP on the test set at different steps for various HSFA layers. HSFA0 corresponds to the use of only simple attention, convolution, and linear layers. It can be observed that the HSFA0 model hardly converges to a satisfactory value, and the loss decreases very slowly. For HSFA3 and HSFA7, the convergence speed of HSFA7 is noticeably faster than that of HSFA3. However, the final results are not significantly different between the two. Therefore, in consideration of the trade-off between performance and speed, HSFA3 is preferred.

Table 7 summarizes the final results. It can be seen that HSFA7 achieves the best training loss, reaching 0.82, and also obtains the highest AP on the test set at 95.4%, which is one percentage point higher than HSFA3 and more than 50 percentage points higher than HSFA0.

Models	Training Loss	AP (%)
0 layer HSFA	1.96	44.0
3 layer HSFA	0.86	94.6
7 layer HSFA	0.82	95.4

Table 7: SOM with different layer of HSFA, training on sub-datasets of LMO, LM, YCBV, HB, TLESS, TUDL, TYOL, only training 20 epoches.

Ablation on Dino module in SOM The experimental settings remained the same as before. In this module, we primarily compared the impact of fine-tuning DinoV2 on our proposed framework. As shown in Fig. 8, fine-tuning DinoV2 does not provide any substantial improvement to the overall performance of our architecture. Both the convergence speed and model robustness remain consistent regardless of whether fine-tuning is applied. Therefore, fine-tuning DinoV2 is not a critical factor in our system.



Figure 7: To provide a comprehensive comparison, we evaluated the training loss, training EMA loss, and test set AP for HSFA0, HSFA3, and HSFAT layers under the same experimental conditions.

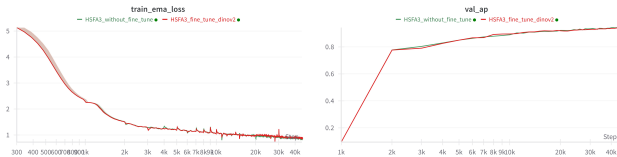


Figure 8: We conducted an ablation study to compare the effects of fine-tuning DinoV2 versus not fine-tuning it. Specifically, we compared the training EMA loss and the AP on the test set under both conditions.

F Tracking Dataset

The training dataset is constructed using BOP as the source. For each object, we extract ground-truth masks to build a memory pool of clean object crops. As shown in Figure. 9, Positive samples consist of segmented images and cropped images from the same object, serving as correctly tracked inputs for the classifier. Negative samples are generated in two ways: (i) pairing segmented images and crops from *different* objects to simulate object identity confusion; and (ii) simulating tracking drift by pairing the segmented images with either randomly shifted crop regions around the mask or randomly cropped image regions. For the training set, we uniformly sample each object at random to generate 100,000 positive pairs. We then apply the same random sampling produce 100,000 negative pairs, yielding a total of 200,000 data pairs. This carefully designed training strategy enables TOM to learn subtle visual cues distinguishing successful tracking from failure cases.

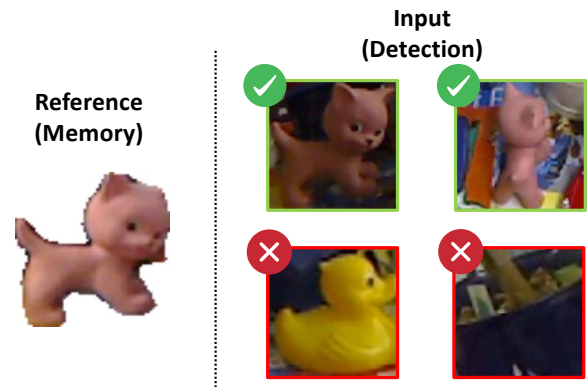


Figure 9: An overview of our tracking dataset. The task is to identify if the input from the detection model *i.e.* the tracked object matches the reference object, which is stored in the memory pool.